ELSEVIER

Journal of Fluids and Structures 20 (2005) 673–695

JOURNAL OF FLUIDS AND STRUCTURES

www.elsevier.com/locate/jfs

Flow structures in the near-wake of the Ahmed model

G. Vino*, S. Watkins, P. Mousley, J. Watmuff, S. Prasad

School of Aerospace, Mechanical and Manufacturing Engineering, RMIT, Melbourne, Australia

Received 14 June 2004; accepted 19 March 2005

Abstract

The time-averaged and time-dependent nature of the Ahmed model near- and far-wake has been investigated experimentally. The use of a new multi-hole probe allowed for measurement in regions exhibiting large flow angles (including flow reversals), and high levels of unsteadiness, allowing examination of flow regions previously difficult to investigate. Although time-averaged results of the far-wake showed good agreement with previously published work, the near-wake structure was found to be somewhat different, with much of the inconsistency being found in the interaction between a separated region over the slant and the recirculatory flows behind the model. Time-dependant analysis revealed that the shedding behind the model is analogous to vortex shedding behind bluff bodies, with most of the fluctuations confined to the axial direction. In addition, the shedding characteristics on the slant showed very similar behaviour to the vertical base, indicating strong turbulent mixing between the two regions, emphasizing time-averaged findings.

1. Introduction

There exists a large database of information directed towards understanding flow structures in the wake of simplified passenger vehicle geometries. Until recently, the bulk of literature has only been successful in elucidating regions in the wake where the flow direction is dominantly in the streamwise sense. In addition, much of this work has been limited to time-averaged behaviour, due to the complexity associated with time-varying flows that exhibit significant flow angles, and sometime complete reversals. The purpose of this research is to further the understanding of flow in the near-wake of a well-known simplified passenger vehicle geometry, in particular regions of complex flows that exhibit both time-averaged and unsteady features.

As highlighted in a review by Le Good and Garry (2004), the use of simplified forms of passenger vehicles has proven extremely useful in terms of understanding the fundamental flow characteristics associated with more complex passenger cars. Although many types of simplified passenger vehicle geometries have been investigated, one of the most popular has been the Ahmed model (see Figs. 1 and 4), after Ahmed et al. (1984). In order to generate flow structures typical of passenger cars, with emphasis on wake flows, this particular shape had a rounded front end to minimize separation and a long mid-section to reduce forebody flow effects on the wake region. The rear end was box-shaped, with several top slant angles investigated.

*Corresponding author.
E-mail address: gioacchino.vino@optusnet.com.au (G. Vino).

0889-9746/$ - see front matter © 2005 Elsevier Ltd. All rights reserved.
doi:10.1016/j.jfluidstructs.2005.03.006

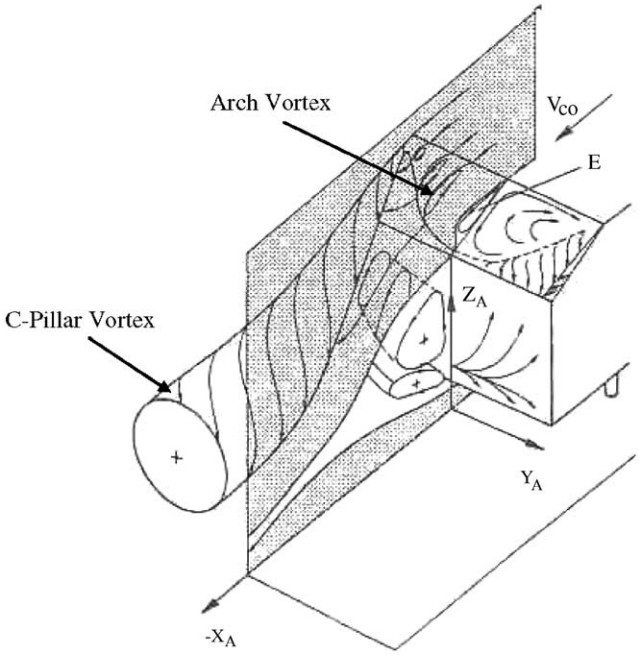

Fig. 1. Proposed vortex system for hatchbacks, after Ahmed et al. (1984).

Ahmed et al. observed that for a base slant angle less than 30°, a separating shear layer turns up from the sides of the rear slanted edge (or C-pillar) and rolls into two longitudinal vortices. Also, the flow separates from the roof-backlight junction and then reattaches on the slant near the vertical base, forming an arch-shaped separation bubble over the backlight. Upon leaving the rear of the backlight, the flow again separates from the top and bottom edges of the vertical base, forming a large recirculatory flow region behind the vertical base. This region exhibits significant levels of flow reversal, and is characterized by two separation bubbles, one above the other and in opposing directions. Fig. 1 shows the proposed vortex system.

Longitudinal vortices were found to depend on the base slant angle. As the base slant angle reaches 30°, the separated bubble on the slanted edge grows in size forming a dominant low-pressure arch vortex on the backlight. This low-pressure region then draws in and strengthens the C-pillar vortices. Overall, the base pressure is significantly reduced, resulting in a significant rise in drag. Beyond 30°, the separated flow is no longer able to reattach down the slanted edge, thus reducing the strength of the C-pillar vortices. Hence, at slant angles above 30° the flow pattern is accompanied by a significant rise in base pressure and therefore reduction in drag.

The ''critical'' 30° backlight configuration was used in this investigation due to the inherent sensitivity in flow topology.

Using the same idealized geometry, Sims-Williams (2001) conducted a detailed study on the time-averaged and unsteady flow structures associated with the critical geometry. The critical configuration was utilized for similar reasons as in this work, in that the flow structures, and therefore drag force, were found to be particularly sensitive to very small changes in backlight angle. Using a smoke flow visualization technique, Sims-Williams demonstrated the sensitivity of the flow pattern near this critical backlight angle. When the tunnel was started up from rest, the flow would be in the low drag state, and then it would switch to the high drag state after several minutes and persist indefinitely. The lower the freestream speed, the longer that the low drag flow state would exist. Fig. 2 shows the two flow states existing at the same backlight angle.

Sims-Williams (2001) also found that, in their time-averaged form, results agreed with those obtained by Ahmed et al. in that the flow structure was dominated by the two C-pillar vortices, which are drawn down towards the ground. Time-accurate data showed that high levels of unsteadiness also existed in the wake, with the highest levels located around the periphery of the C-pillar vortices. It was revealed that these regions of high unsteadiness were associated with a distinct

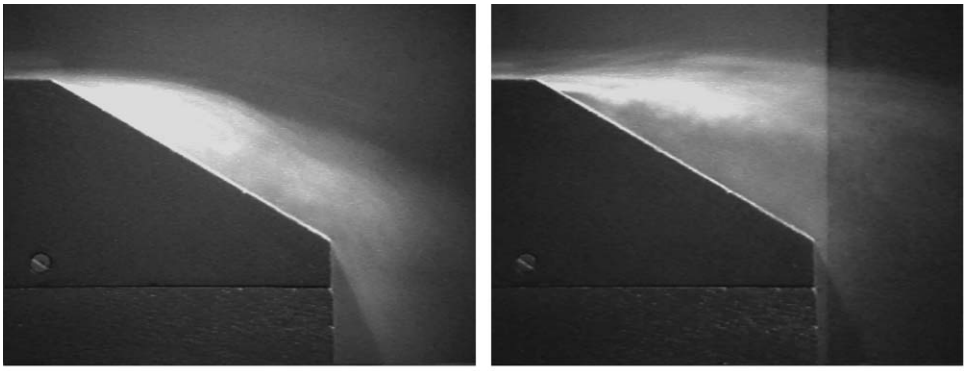

Fig. 2. High- and low-drag flow structures at the same backlight angle of 30°, after Sims-Williams (2001).

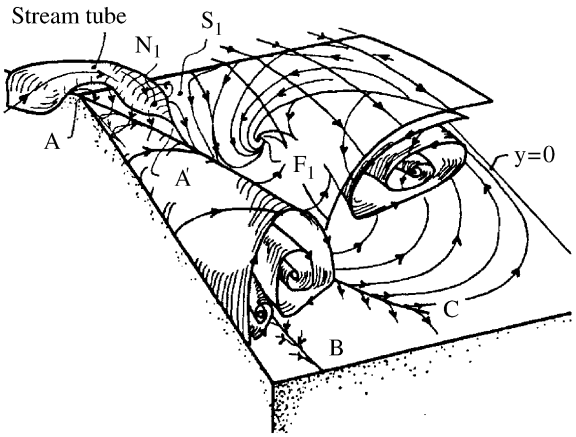

Fig. 3. Flow pattern over slanted edge of Ahmed model, after Spohn and Gillieron (2002).

shedding frequency, giving a Strouhal number of about 0.35 (based on square-root of the frontal area[1]). However, due to limitations associated with instrumentation, Sims-Williams was unable to investigate the flow field very close to the model surface (i.e. regions of large flow angles), and therefore, was unable to completely describe the complex behaviour in the near-wake.

In a more recent study, Spohn and Gillieron (2002) were also able to show the complex flow phenomena occurring around the Ahmed model shape via an off-body flow visualization water tunnel based technique (see Fig. 3).

Although their work was focused solely on the 25° backlight angle configuration, they too found that the near-wake was dominated by a set of counter-rotating (lifting) trailing vortices, which bounded a central separation bubble that enclosed a flow reversal region. However, unlike the work of Ahmed et al. (1984) they showed that the detached flow region on the slant did not reattach prior to reaching the vertical rear base of the model, but mixed with the flow in the wake. Within this separated region above the slant existed two radiating foci F_1 (one on each side of the model) situated near the top corners of the slanted edge, which caused the reverse flows inside the bubble to take a radiating path back toward the foci origins. This result helps explain the hypothesized skin friction patterns of Ahmed et al., who showed a similar result through surface flow visualization, although were unable to show the existence of the stable focus. Fig. 3 shows the flow topology on the slanted edge of the Ahmed model proposed by Spohn and Gillieron. The line AB

[1]Given that the Ahmed model is a relatively 'bluff' body, resulting wake patterns will be highly dependent on its cross-sectional characteristics rather than its length and as such, Sims-Williams based Strouhal number calculation on a characteristic length equal to the square root of frontal area.

corresponds to the separation of a secondary vortex generated between the main trailing vortex and the c-pillar, while A′C represents the attachment of the main vortex.

Nouzawa et al. (1992) extended an earlier investigation with an unsteady analysis of a notchback model shape. They observed that an arch vortex (initially found on the rear window and deck-lid of an earlier study) exhibited significant unsteady characteristics. Through hot-wire and surface pressure measurements, they found that the arch vortex sheds from the model at a frequency of 20–30 Hz (corresponding to a Strouhal number, also based on square-root of the frontal area, of about 0.37–0.55) in an alternate fashion from each side of the rear window. This characteristic frequency compared well to fluctuations observed in drag measurements, indicating that this vortex structure governs much of the aerodynamic characteristics.

Through the use of PIV, Wang et al. (1996) were able to illustrate the significant differences between time-averaged and unsteady flow structures in the wake of a fastback vehicle shape. For a transverse plane taken behind the model, they found that the instantaneous flowfield consisted of several 'small' vortices quite evenly distributed throughout the traversing plane, while the time-averaged counterpart appeared to have 'diffused' much of the small pockets of vorticity and consisted of mainly two large contra-rotating trailing vortices.

Overall, it is evident that the complex flow structures associated with the wake of passenger cars continue to be a fruitful area of research, particularly where unsteady phenomena occur. This paper will attempt to add to the current body of knowledge through a detailed experimental investigation into the time averaged and unsteady near-wake of the Ahmed model.

2. Experimental arrangement

2.1. Test model

The Ahmed model used here was equivalent to a $\frac{1}{4}$ scale, giving it a length, height and width of 1044, 288, and 389 mm respectively. The slant angle was held constant at 30°. Refer to Fig. 4.

2.2. Drag measurements

Time-averaged forces were measured using a six-component strain gauge balance mounted inside the test model via a sting mount. The force sensor used was supplied fully calibrated by JR3 Inc., although calibration checks were conducted between each run. The maximum error in drag associated with repeatability and hysteresis was found to be approximately $\pm 2.1\%$.

2.3. Smoke flow visualization

Smoke flow visualization tests were conducted at a freestream speed of 7 m/s, corresponding to a Reynolds number of 4.4×10^5 based on model length. Although this value of Reynolds number is considerably lower than the majority of research conducted on the Ahmed model geometry, the present work (see Fig. 11) suggests that the overall flow

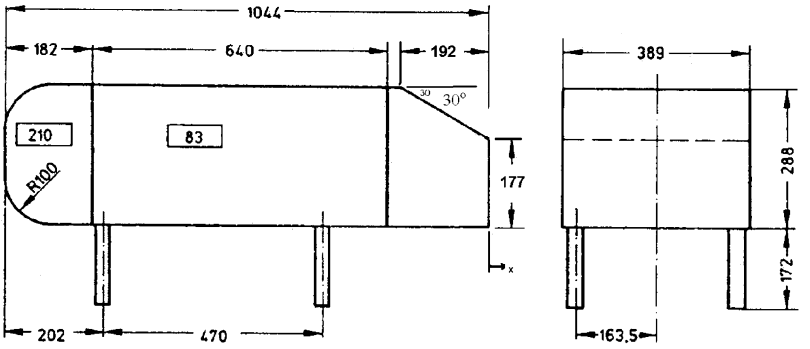

Fig. 4. Test model, after Ahmed et al. (1984).

structure does not change significantly with tunnel speed, mainly due to the model having sharp edges at the rear end, thus the location of separations will not change with flow speed.

However, Sims-Williams (2001) was able to show that the flow could be manually switched between high- and low-drag flow structures by using a flat plate to guide the flow onto the slant surface or to force it to separate. When initiated at high Reynolds numbers ($>5.9\times10^5$), the low drag flow structure could be observed for a small amount of time after which would return to the more stable high drag state, although when initiated at Reynolds numbers below 4.7×10^5, the low drag structure could be maintained for several minutes.

The work Spohn and Gillieron (2002), which was conducted in a water tunnel at a Reynolds number of 3×10^4, also suggests that the Ahmed model exhibits small changes in flow characteristics as a function of Reynolds number.

2.4. Surface oil flow visualization

Surface skin friction patterns were obtained by 'painting' the surface with a solution of fine powder (Paraffin) and a carrier (Kerosene), which enabled the visualization of shear stress direction over the model surface. The wind tunnel was run at 30 m/s, corresponding to a Reynolds number of 2.1×10^6. Still pictures of the final flow patterns were taken with the wind tunnel turned off to show the 'time-averaged' surface shear stress patterns.

2.5. Surface pressure measurements

Time-averaged and time-varying surface pressure measurements were conducted at a range of speeds between 20 and 35 m/s. In order to measure time-accurate surface pressures on the model, a dynamic pressure measurement system was used. Time-accurate surface pressures can provide valuable information about the wake of a passenger vehicle, as this is the region where the majority of flow phenomena originate. The most important use for time-accurate pressures is that they can be used to obtain spectral estimates and therefore determine areas which exhibit periodic phenomena. To obtain a secure stationary signal, all surface pressure and flow field time-varying data were obtained from 60-s samples, sampled at a frequency of 625 Hz.

The Dynamic Pressure Measurement System, which was supplied by Turbulent Flow Instrumentation Pty Ltd, consists of a number of pressure modules that connect to a data acquisition system. Each pressure module features fifteen pressure ports (each connected to a high-frequency pressure transducer) a reference pressure port that is common to all transducers and an output connector.

Silicone tubes of 0.8 mm diameter were inserted at each surface pressure tap and connected to the pressure modules. As all silicone tubes were the same length, a single tubing transfer function (see later for technique used to correct for pressure variation in the silicone tubing) was applied to all measured signals.

2.5.1. Dynamic pressure correction and frequency response

Ideally, high frequency response pressure measurement systems would have pressure transducers located at the point of measurement. However, since this is not practical with current transducer sizes, pressure taps were connected to transducers via silicone tubing. As described by Iberall (1950), the oscillatory pressures through these tubes undergo an amplitude variation and phase lag that is frequency dependent. Therefore, the pressure signals measured by the transducers must be linearized to correct for the amplitude and phase distortion.

The correction used here, which is based on a Fourier transform technique, has been applied with much success [i.e. Hooper and Musgrove (1997), Sims-Williams and Dominy (1998) and Mousley et al. (1998)]. The technique consists of obtaining the Fourier transform of the measured signal at the transducer, dividing this by a complex transfer function (that relates the dynamic pressure amplitude and phase delay at the transducer to that at the point of measurement), and transforming the result back to the time domain via an inverse Fourier transform. The tubing transfer function is obtained either experimentally or via a theoretical technique, with the latter being used in this investigation.

The theoretical prediction of the response characteristics of various tubing systems, which was first derived by Bergh and Tidjeman (1965), is based on derivations from the Navier–Stokes equations, continuity equation, the equation of state and the energy equation. Results have shown good comparison to experimentally obtained tubing response transfer functions [see Bergh and Tidjeman (1965), Hooper and Musgrove (1997), Mousley et al. (1998) and Gilhome et al. (2001)].

For the tubing size of 0.8 mm diameter and 370 mm length used in this investigation, the calculated transfer functions of amplitude and phase distortion are shown in Fig. 5.

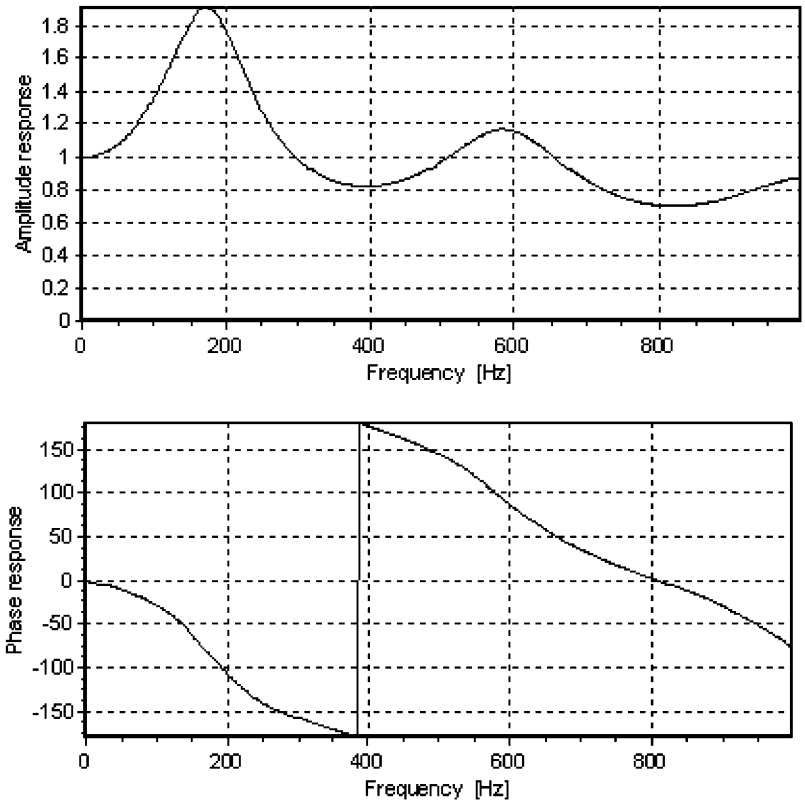

Fig. 5. Amplitude and phase response of silicone tubing used for surface pressure measurements.

2.6. Flow field measurements

In order to obtain a more complete representation of the flow field, off-body flow measurements were taken at three downstream transverse planes in the wake of the model.

Researchers have gone to extraordinary lengths to develop complex experimental techniques to obtain measurements in regions where significant flow reversal occurs. For example, Watmuff et al. (1983) describe the construction of an air-bearing sled that is propelled back and forth continually above the working section of a wind tunnel. A sting attached to the sled supports a crossed-wire probe and the superimposed bias velocity imposed by upstream motion of the probe reduces the range of cone angles made by the velocity vector relative to probe axis. If the bias velocity is large enough, then valid measurements can also be obtained in regions of reversed flow without the usual problems of directional ambiguity. Perry and Watmuff (1981) exploited this capability to obtain measurements in the turbulent separation bubble located behind an ellipsoid. In order to obtain measurements at a high enough velocity close to the surface of the ellipsoid, they devised a mechanism whereby the ellipsoid splits in two at the last instant to allow the probe to pass through.

In this study, single point flow measurements were conducted at a wind tunnel speed of 35 m/s using a 13-hole, high frequency response pressure probe. Vertical and horizontal grid spacing between measurement points was kept constant at 30 mm to maintain good resolution. Fig. 6 shows the locations of these planes (Note: L = model length).

This pressure probe, known as the extended cone of acceptance (ECA) Probe, was supplied by Turbulent Flow Instrumentation (Fig. 7). It is of the multi-hole type and has a flow acceptance cone of about $\pm 135^{\circ}$, resolving all three components of velocity and local static pressure up to frequencies of about 1 kHz. Regions outside the flow accepted cone are associated with the probe stem, connecting the head to the main body. The probe houses the pressure transducers and other electronics within the main body, and has a length of 250 mm, maximum body diameter of 20 mm and a probe head (located 80 mm away from the main body) diameter of 6 mm.

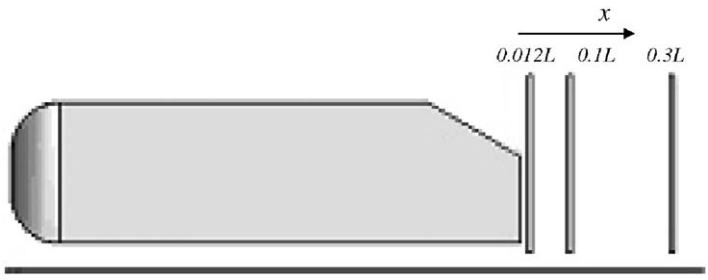

Fig. 6. Locations of measurement planes in wake of Ahmed model.

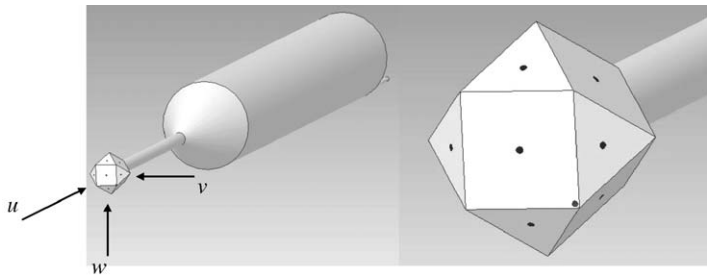

Fig. 7. 13-hole ECA Probe.

The steady state calibration of the ECA Probe is performed in a similar manner to that of Hooper and Musgrove (1997). The calibration relates the pressure field detected by each of the 13 pressure taps on the faceted head to the magnitude of the instantaneous local velocity vector and the flow yaw and pitch angles defined as dimensionless pressure ratios. The flow over the calibration surface is divided into a number of zones, each with its own set of calibration coefficients, or 'surfaces', which are derived from ratios of pressures of the thirteen holes. The calibration procedure was conducted over pitch and yaw angle ranges from $\pm 135^\circ$ in 3° increments in a relatively smooth flow (i.e. $I_{uu} < 1\%$). In addition, the full ranges of calibration were performed at several velocities in order to quantify and correct for variations due to Reynolds number change.

As for the dynamic pressure measurement system, oscillatory pressures through tubes also undergo amplitude and phase changes that are frequency dependant. Using the same method as for the dynamic pressure measurement system, the pressure signals measured by the transducers in the probe body are linearized. The tubing used was 0.3 mm hypodermic, resulting in the transfer functions of amplitude and phase distortion shown in Fig. 8.

It is evident that the smaller tube size of the ECA Probe induces stronger pressure attenuation over the frequency band compared to the larger tube used in surface pressure measurements. Thus, the frequency response of the ECA Probe is limited to approximately 1 kHz.

In order to capture all flow angles associated with regions very close to the rear of the model, the probe was misaligned from its customary direction (i.e. probe head pointing into the freestream) and reoriented at 90° to the freestream. This allowed for measurements of completely reversed flows and minimized the effects of the probe body on flow reversals. Test results indicated that at very close distances from the rear of the model, a minimum of 91% of the data fell inside the calibration surface of the probe during sampling.

Since the ECA Probe is a relatively new flow-measuring device, the authors conducted a detailed validation study in various flows including smooth, turbulent and swirling flows, all of which are common flows in bluff body wakes. Results were compared to measurements from an already well-established turbulence-measuring tool, the four-hole Cobra probe [see Hooper and Musgrove (1997) and Chen et al. (2000)] and showed excellent agreement. A small portion of the data obtained during this validation is discussed below.

In order to assess the reverse flow capabilities, tests that exposed all 13 pressure taps to the oncoming freestream were conducted. A freestream speed of 26 m/s was used with the head of the ECA Probe placed at the same location in space and misaligned through variation of pitch and roll angles from 0° to 120° and 0° to 360° respectively. Comparisons to reference probe measurements showed a maximum deviation of $\pm 0.5\%$ in mean axial velocity when compared with the

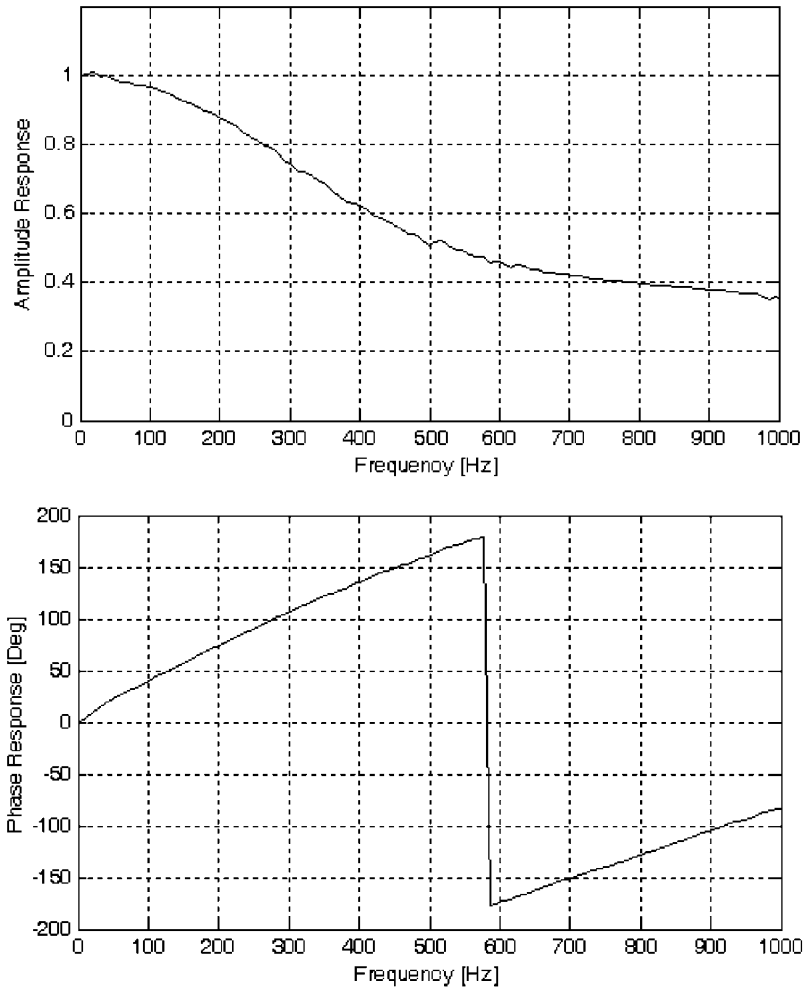

Fig. 8. Experimental amplitude and phase lag response of tubing inside ECA Probe, courtesy of TFI.

ECA Probe in its conventional (zero pitch and yaw) orientation. Once local measured velocities u, v, and w were resolved back to a coordinate system aligned with the mean flow direction, the largest deviations were found to occur when the probe was pitched and axially rolled at 120° and 270°, respectively. This error in mean velocity was found to be $\pm 2\%$ of freestream speed and angular deviation in pitch and yaw angles was within $\pm 2°$.

Fig. 9 presents data obtained during Reynolds number sensitivity checks in a low turbulence flow, in which hot-wire anemometer results showed a turbulence intensity, I_{uu}, of 1.6% at 15 m/s dropping to 1.5% at 30 m/s. Clearly, both probes demonstrate good agreement with each other and hot-wire results. The maximum variation in turbulence intensity between the two probes was 0.31%, which occurred for the transverse component of turbulence intensity, I_{vv}, at a speed of 30 m/s.

Frequency response capabilities were also investigated in order to give confidence of accuracy in highly turbulent flows. Fig. 10 presents an auto-spectral density plot taken from fluctuating vertical velocity signals of the Cobra and 13-Hole Probes in the wake of a circular cylinder. Both plots show a well-defined spectral peak centered about 54 Hz, which corresponds to a Strouhal number of 0.2 based on cylinder diameter. The ECA Probe also shows good agreement with the Cobra Probe over the entire frequency band.

Overall, the validation exercise indicated that the accuracy of the 13-Hole ECA Probe is satisfactory for measurements in both steady and unsteady flows exhibiting large flow angles (including complete flow reversal). However, the reader should note that limitations are associated with the probe in certain flows, particularly for areas exhibiting very small local velocities (~2 m/s). In addition, due to the intrusive nature of the probe, spatial resolution

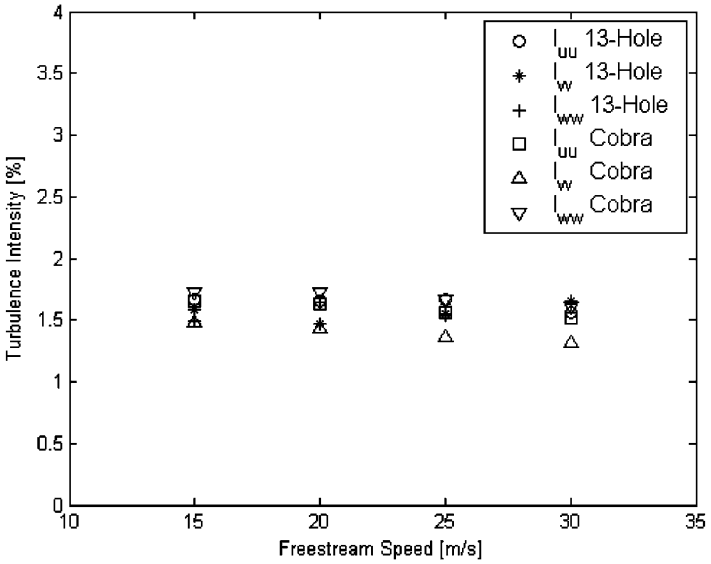

Fig. 9. Variation of measured turbulence intensity with test speed for both the 13-hole and Cobra probes.

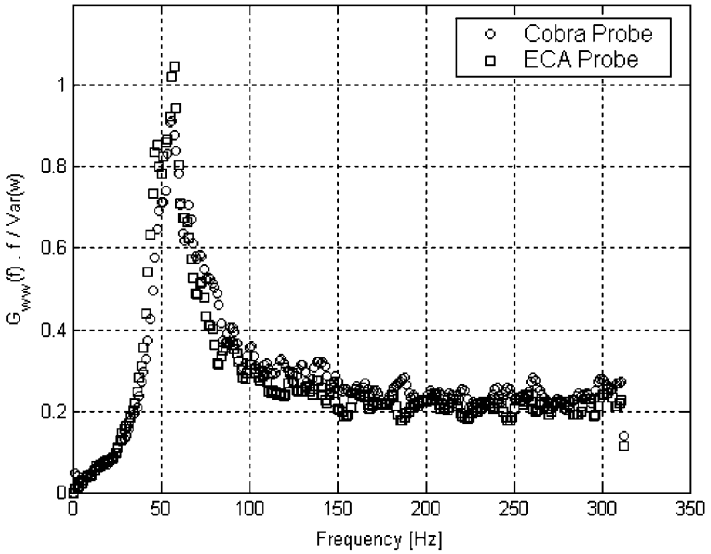

Fig. 10. Comparison of auto-spectral density taken from fluctuating vertical velocity signals of the Cobra and 13-Hole Probes in the wake of a circular cylinder.

limits measurements to flows not exhibiting large local pressure gradients (i.e. thin shear layers). A more detailed description of the ECA Probe and its capabilities underlining experimental verification is given in Vino and Watkins (2004).

2.7. Wind tunnel

All tests in this investigation were conducted in the RMIT Industrial Wind Tunnel. The wind tunnel is a closed-jet and fixed-ground type, and is able to generate flow speeds of up to 43 m/s, corresponding to a longitudinal turbulence intensity of 1.53%. The wind-tunnel blockage ratio was equal to 1.9%, based on maximum projected frontal area of the

Ahmed model, which was deemed suitable in that relevant flow structures would not be significantly affected by the presence of the wind tunnel walls. No corrections were made for blockage.

3. Results

3.1. Time-averaged results

Fig. 11 shows the influence of Reynolds number on the drag coefficient of the Ahmed model for test speeds ranging from 11.1 to 41.25 m/s, corresponding to a Reynolds number range (based on model length) of $0.763 \times 10^6 < \mathrm{Re} < 2.83 \times 10^6$. Although the model is quite bluff, it is apparent that the drag characteristics are affected by changes in Reynolds number. Drag is at its highest at very low speeds and gradually decreases with increasing Reynolds number.

At a Reynolds number of about 2.5×10^6, the distribution approaches a minimum pertaining to a drag coefficient of about 0.316, after which the drag gradually rises back to a value of 0.33 at a Reynolds number of 2.83×10^6. It is worth mentioning that this value of drag coefficient is somewhat smaller than the value of 0.378 obtained by Ahmed et al. (1984). However, although Ahmed et al. used the same scale model, their results were obtained at a freestream speed of 60 m/s, corresponding to a test Reynolds number of 4.1×10^6. On closer inspection, it appears as though the drag rise at higher Reynolds numbers is gradually approaching the Ahmed et al. value of 0.378.

To assess whether these Reynolds number effects were related to transition of the boundary layer on the model forebody from laminar to turbulent, tests were also conducted with boundary layer trips in place to ensure the presence of a turbulent boundary layer. The strips were made of 3 mm wide and 2 mm thick roughened aluminium, and spanned across the entire model forebody. Results showed no discernable effects with the trips in place, indicating the presence of a fully turbulent boundary over all model surfaces. The results shown in Fig. 11, for $\mathrm{Re} < 2.5 \times 10^6$, seem to complement this conclusion since with increasing Reynolds number, the thickness of the turbulent boundary layer on the flat midsections is reduced, therefore accompanied by a reduction in skin friction drag [see Schlicting (1960)]. Since Reynolds numbers higher than 2.83×10^6 were unattainable and the data show a trend of increasing drag coefficient at the higher end of the tested range, it was difficult to predict the drag behaviour beyond this point. Thus, it is impossible to determine whether this trend would continue or if drag would stabilize soon after. Therefore the authors are reluctant to make explicit conclusions as to the source of the gradual drag rise for $\mathrm{Re} > 2.5 \times 10^6$.

Fig. 12 shows the off-body flow patterns at the rear of the model. In Fig. 12(a) the smoke was injected at the end of the roof centerline, while the smoke patterns shown in Fig. 12(b) originated at the top of the C-pillar as shown. The wake pattern shows excellent agreement with that of Sims-Williams (2001), in that the flow over the backlight shows a large separation bubble over the entire centerline, consequently aiding the generation of a strong trailing vortex from the C-pillar, which is very well-defined.

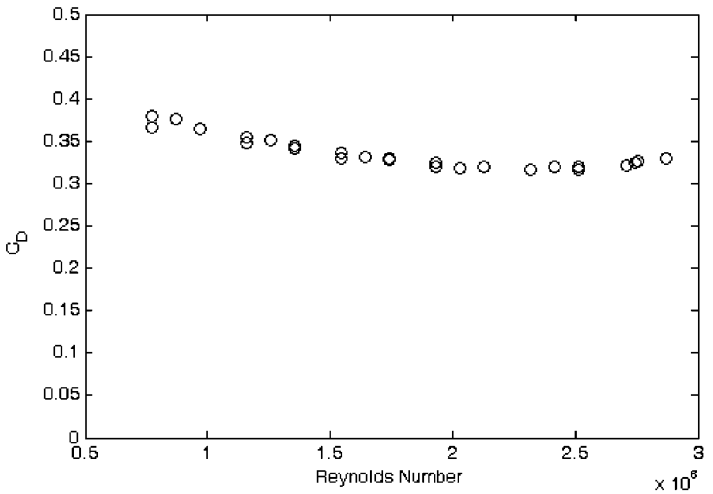

Fig. 11. Reynolds number effects on Ahmed model geometry.

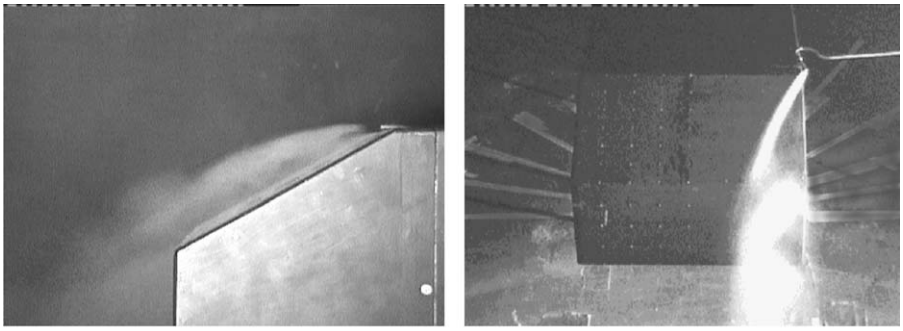

Fig. 12. Off-body smoke flow patterns at rear end of the model.

Fig. 13. Rear end surface skin friction patterns.

It appears as though the detached flow over the slanted edge does not reattach before the base. In fact, the bulk of the injected smoke over the slant remains well away from the surface, with only faint areas of smoke appearing close to the body. In addition, it is clear that this faint region of smoke close to the slant surface vacates into the separated region behind the vertical base. This is in contrast to the flow topology suggested by Ahmed et al. (1984), who proposed that flow above the central region of the slant is characterized by a large separation bubble that reattaches before separating again at the base. Our finding agrees with the work of Spohn and Gillieron (2002), who also found that the detached flow region on the slant was not closed but mixed with the flow in the wake. It is important to note that the model used by Spohn and Gillieron had a slant angle of just 25°, which would only act to promote reattachment.

Fig. 13 shows the corresponding surface skin friction streamlines on the backlight and vertical base, which reveal several important flow features. Firstly, the flow from the roof separates at the top of the backlight, which is consistent with smoke flow patterns. Just inboard of the C-pillars, there exists a separation line extending through the entire length of the backlight. This line makes an angle of approximately 7° relative to the C-pillar, comparing well to results obtained by Sims-Williams (2001) and Ahmed et al. (1984). It has been widely accepted that this separation line is a result of the C-pillar vortex separating as it spirals along the backlight.

Further inboard there is a large separated region that extends to the base of the backlight. Many authors have also revealed the existence of this large separated region, which is bordered by the trailing vortex impingement lines. These impingement lines also agree with smoke patterns shown in Fig. 12.

Within this region exist significant levels of reverse flow in a radiating pattern originating from a main stable foci located just below the top corners of the backlight. The presence of these foci corresponds to the work of Spohn and Gillieron (2002), although their location appears to be a lot closer to the roofline. These foci were not mentioned in the work of Ahmed et al. but their hypothesized skin friction patterns did show a similar pattern of radiating flow reversals,

thus implying their presence. In addition, unlike the work of Ahmed et al. (1984), whereby this reverse flow region was fully enclosed and assumed an arch shape, this region takes on a 'D-like' shape, with a central tail at its base. This central tail, which is relatively thin (32 mm wide at the base), does not show any sign of reattachment but instead exhibits flow reversals right up until the rear of the model. A similarly shaped detached flow region was also found by Sims-Williams (2001). Thus, it is envisaged that the separated flow over the slant reattaches along the vortex impingement lines, but not in the small region between, comparing well to smoke flow patterns.

The overall flow pattern on the slant appears slightly asymmetric, which is attributed to errors in model alignment and/or uneven distribution of applied solution.

On the vertical base, there exists a well-defined line that makes the shape of an arch. Skin friction patterns suggest that the flow originates at the periphery of this arch and radiates towards the top and sides of the base. Within the arch, patterns made during model preparation are significant, indicating low levels of energy within this region. This suggests that the flow just off the surface of the vertical base is characterized by a dominant recirculation bubble, taking the shape of an arch. It is envisaged that a counter-rotating vortex is created below, which is fed by the flow coming from the underbody and this large arch vortex, although this is not discernable from Fig. 13.

Fig. 14 shows the corresponding time-averaged contour plot of surface pressure coefficient (based on freestream speed) for one-half (r.h.s.) of the model rear end.

Fig. 14 shows that the slanted surface is characterized by large pressure gradients. In the upper central region of the slant, pressures are at their minimum due to the high-momentum flow leaving the roof of the model and rise sharply due a sudden change in geometry. This positive pressure gradient consequently induces a separation immediately aft of the roofline, which extends out very near to the C-pillars. The distinct region of low pressure towards the C-pillar suggests that separation is delayed in this area. This is attributed to the presence of the trailing vortex (evident by the region of local low-pressure along much of the C-pillar), which acts to 'energize' the flow, thus delaying separation. Further inboard, a thin region of local high pressure is observed, which coincides with the main trailing vortex impingement observed in surface streamline pattern in Fig. 13. The vertical base, however, is characterized by a single region of low pressure, with little evidence of pressure gradients. Interestingly, the pressures within this region are comparable to those on the centre portion of the slanted edge, complementing observations made from flow visualization results.

Fig. 15 shows the mean velocity vectors measured with the ECA probe along the plane of symmetry and Fig. 16 shows the streamline pattern (streamlines are defined as lines being parallel to the flow direction and as such, were found by integrating along the flow direction following the velocity vectors at each measurement point).

Immediately behind the vertical base, a well-defined separation at the top and bottom of the vertical base is apparent, enclosing a clear recirculatory flow region. Two recirculatory bubbles are observed, one above the other, and in opposing directions. The higher bubble covers the upper region of the vertical base, while the lower bubble, which rotates in the opposite direction, does not appear to interact with the surface. This finding agrees with skin friction patterns of Fig. 13, which indicated that a single recirculation bubble interacted with the vertical rear surface. Both bubbles inside the separated region are bordered by the attachment saddle, at which point the flow from above interacts with the flow coming from the underbody. As the flow travels downstream, the velocity vectors inside the wake gradually turn up towards the streamwise direction. The corresponding axial velocity contour is shown in Fig. 17.

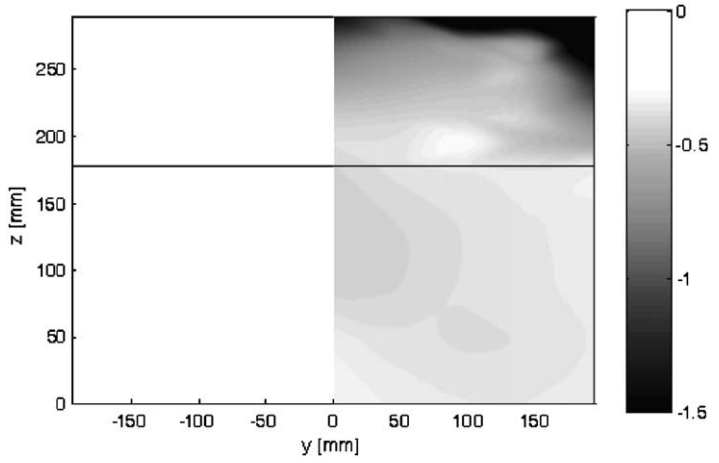

Fig. 14. Surface pressure coefficient on the model rear end; view from behind.

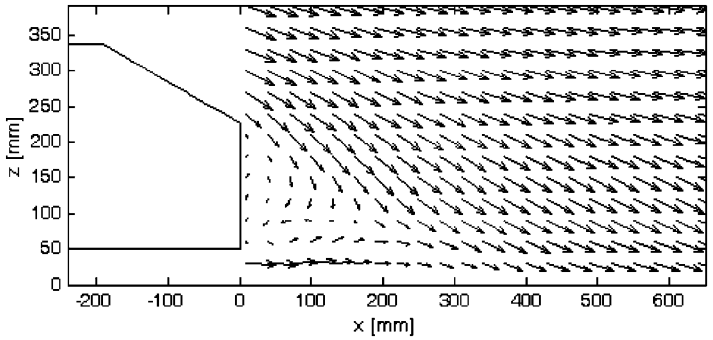

Fig. 15. Velocity vectors measured along the symmetry plane in wake of model.

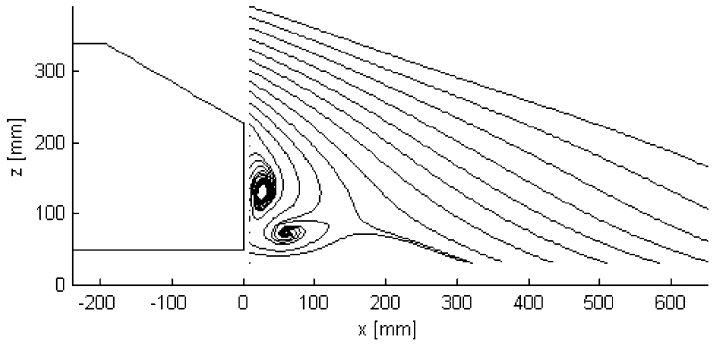

Fig. 16. Integrated streamlines along the symmetry plane in wake of model.

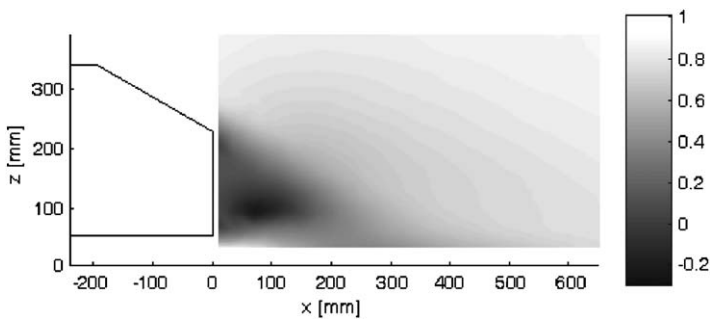

Fig. 17. Streamwise velocity measured in the plane of symmetry in wake of Ahmed model.

Again, the region of flow recirculation is clearly visible, with highest levels of flow reversal located close to the bottom of the vertical base.

Fig. 18 shows time-averaged cross-flow velocity vectors in the wake, obtained from single point measurements with the ECA Probe. Thus far, this complex near-wake flow region has proven difficult to capture due to the limitations associated with hot-wire and pressure probes measuring flow reversals. However, flow structures within this region were successfully captured with the 13-hole probe.

As originally observed by Ahmed et al. (1984) and later by Sims-Williams and Dominy (1998) and Spohn and Gillieron (2002), it is evident that the overall flow is dominated by two strong contra-rotating vortices generated by the C-pillars. Very close to the rear of the model, at $x/L = 0.012$, the separation bubbles on the vertical base are clearly

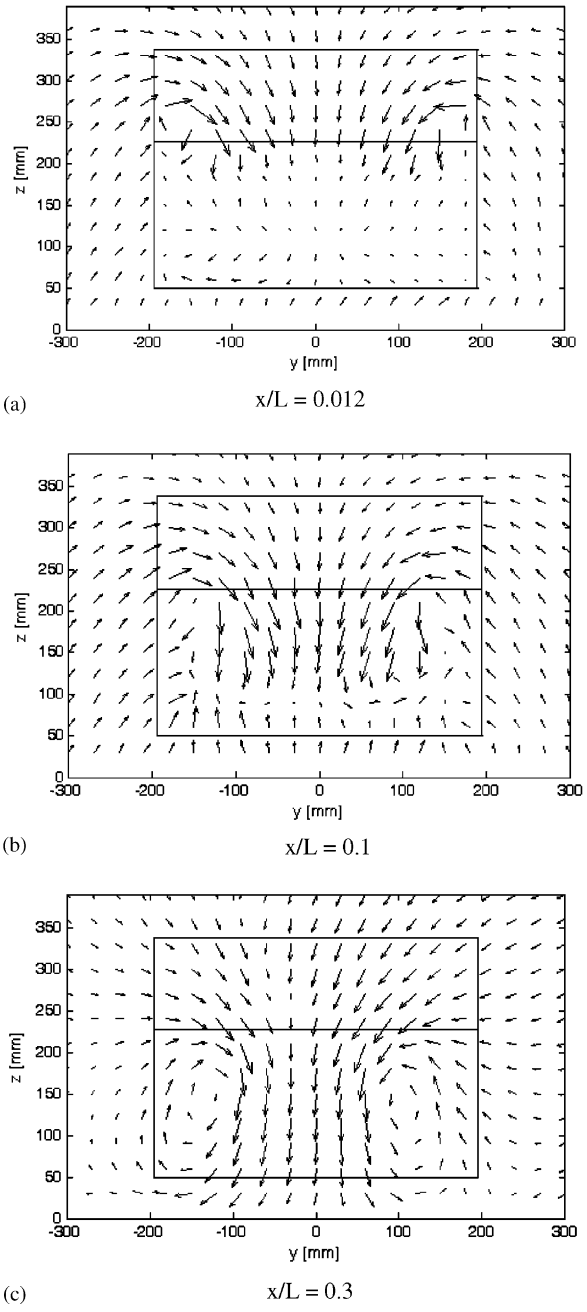

Fig. 18. Cross-flow velocity vectors in wake of Ahmed model at three downstream transverse planes.

seen. As the lower and upper recirculation bubbles are very close to the rear of the model surface, clearly discernable down- and up-wash is seen. It is also clear that the downwash caused by the strong trailing vortices forces the flow leaving the slant to separates at such steep angles (see Fig. 16), steeper than the backlight itself.

Further downstream at $x/L = 0.1$, the vortex cores have moved down and inwards. The upwash from beneath the model is clearly visible, leading toward the stagnation line from which reverse flows originate. It is interesting to note that the region of flow reversal does not extend out near the sides of the model, but is confined to the central region of the base. This suggests that the size of separated region is reduced significantly as it moves downstream. Again, this

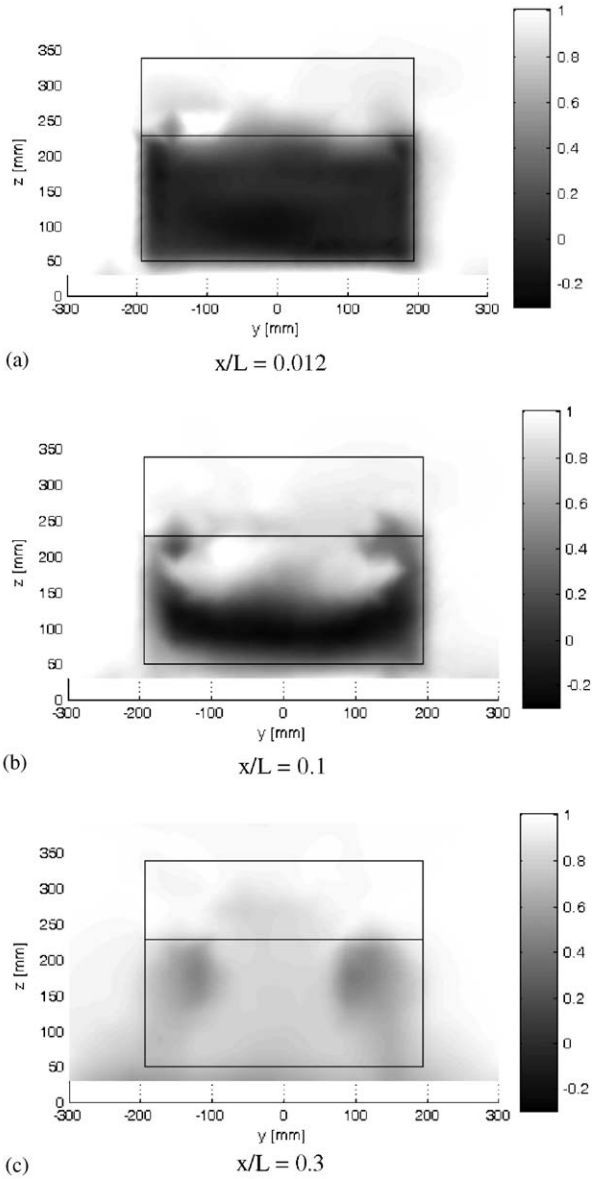

Fig. 19. Streamwise velocity contours in wake of Ahmed model at three downstream transverse planes.

region has previously been difficult to capture, although flow structures proposed by Ahmed et al. (1984) agree in that the flow here is characterized by large separated recirculatory bubbles, one above the other (see Fig. 1 for clarification).

Further downstream, the trailing vortices grow significantly in size while moving closer toward the ground plane. As these vortices interact with the ground plane, they tend to be 'squashed' and widened, causing them to extend out towards the model sides. Corresponding contours of axial component of velocity (normalized by freestream speed) are shown in Fig. 19.

At $x/L = 0.012$, the region of flow recirculation behind the vertical base is well defined, and exhibits evenly distributed flow reversals of up to $0.3U_\infty$, which cover the entire vertical base region. Trailing vortices are faintly evident at each upper corner of the reverse flow region.

Further downstream, the flow reversal region has reduced in size, comparing well to Fig. 18. Here, the trailing vortices are more apparent as they begin to separate from the flow reversal region. However, this recirculatory flow

region does not extend far downstream (as indicated in Fig. 16) as a significant recovery in streamwise velocity is seen in the wake map taken at $x/L = 0.3$. Here, the vortex cores maintain the highest levels of axial velocity deficit.

As a whole, the flow maps reveal the path of the vortex cores, showing that the flow moves down and extends out towards the model sides as it moves downstream.

3.2. Unsteady results

In his unsteady analysis of rear-end surface pressures of a passenger car geometry, Gilhome (2002) was able to distinguish two main regions of distinct spectral activity. He found that regions of low pressure were associated with high levels of unsteadiness or turbulent behaviour, while regions of high pressure were associated with low levels of unsteadiness. Fig. 20 shows the levels of surface pressure coefficient unsteadiness (standard deviation of pressure normalized by freestream dynamic pressure) on the Ahmed model backlight.

Fig. 20 suggests that the majority of surface flow exhibits unsteadiness. The only region that does not appear to have time-varying characteristics is that between the C-pillar vortex impingement line and the model centreline. However, it is important to note that the magnitudes of unsteadiness are relatively low over the majority of the backlight and vertical base. Although not seen in the time-averaged surface pressure contour, the separation bubble seen at the bottom of the vertical base via surface skin friction patterns is strongly represented here, and appears to exhibit relatively high levels of unsteadiness.

Overall, the centreline region of the slant and vertical base appear to exhibit similar time-variant behaviour, indicating that vortex shedding dominates this region. Interestingly, Fig. 14 showed that these two regions also exhibited similar time-averaged characteristics.

Fig. 21 shows corresponding nondimensional spectral characteristics (i.e. auto-spectral density × frequency/variance) of selected surface pressure taps. Interestingly, Fig. 21 shows that both the slanted edge and vertical base exhibit a sensitivity of shedding phenomena, with Strouhal number increasing with Reynolds number. Roshko (1993) notes that rising values in Strouhal number are usually accompanied by falling values in drag coefficient. This corresponds to results shown in Fig. 11, where a reduction in drag coefficient was observed with increasing Reynolds number.

Each spectral estimate shows a single dominant shedding frequency, which corresponds to a Strouhal number between 0.36 and 0.39 (based on the square root of model frontal area), depending on Reynolds number. Readings from pressure taps on both the vertical base and slanted edge indicate high energies are associated with the shedding here, particularly on the upper region of the base.

Fig. 22 shows the correlation between shedding characteristics of the top and bottom recirculatory bubbles found on the vertical base. Firstly, we see that the phase estimate near the nondimensional shedding frequency of 0.39 suggests that the shedding is 180° out of phase, implying alternate shedding. Thus, the recirculatory bubbles located behind the vertical base (see Fig. 16) are analogous to the well-known von Karman vortex shedding behind bluff bodies, particularly square cylinders, shedding alternately at a Strouhal number of about 0.39. For the test speed range used here, Reynolds numbers (based on square root of frontal area) were between $5.5 \times 105 < Re < 7.7 \times 105$. It is known that

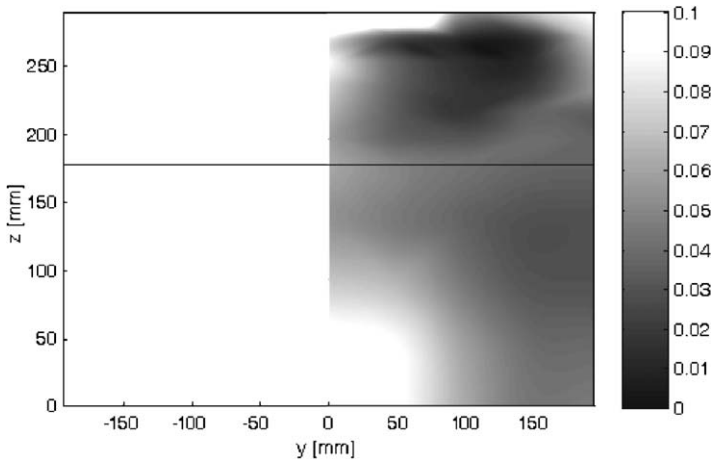

Fig. 20. Backlight surface pressure coefficient unsteadiness.

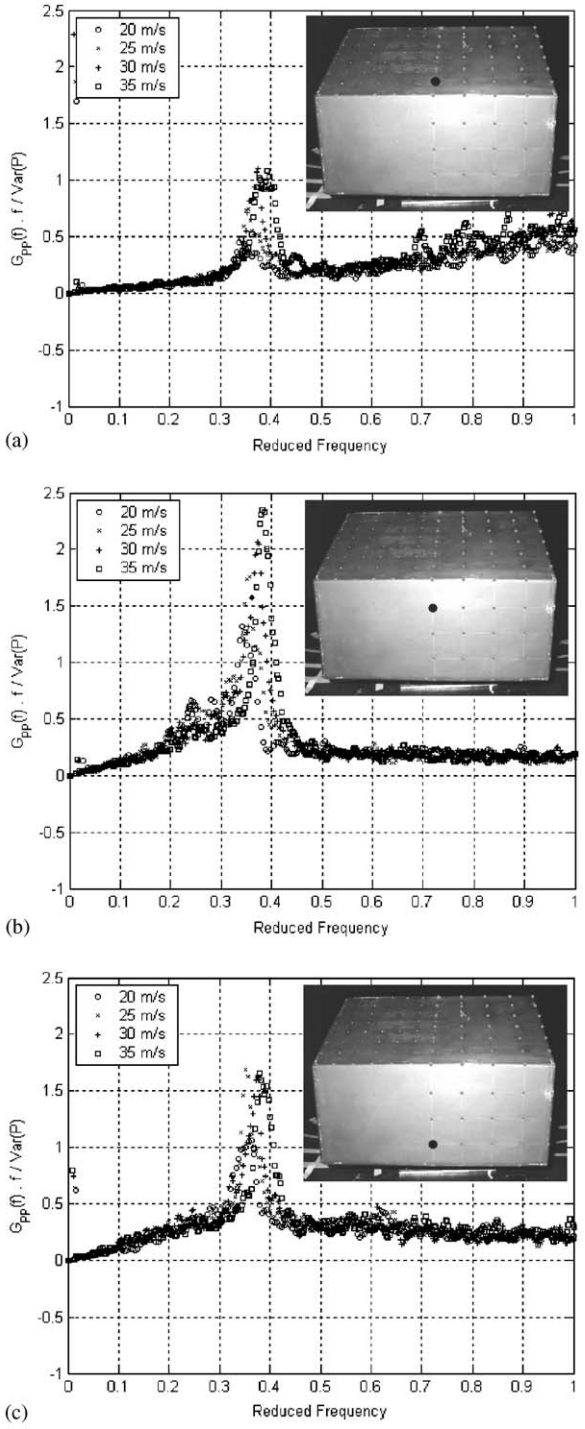

Fig. 21. Nondimensional auto-spectral density functions of selected surface pressure taps on the rear of the model.

at such high Reynolds numbers, circular cylinders exhibit significant losses in periodic flow [see Roshko (1993)] due the boundary layer undergoing transition to turbulent, creating a smaller wake, and accompanied by diminishing shedding characteristics. However, square cylinders tend to exhibit well-defined shedding behaviour up to Reynolds numbers well beyond those investigated here due to the separation locations being fixed on objects with square rear-ends, irrespective

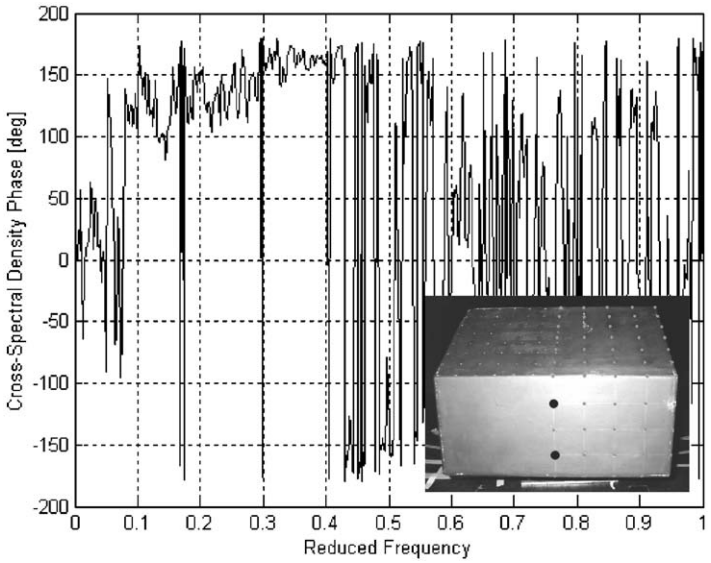

Fig. 22. Cross-spectral phase estimate between selected surface pressure taps on the vertical base.

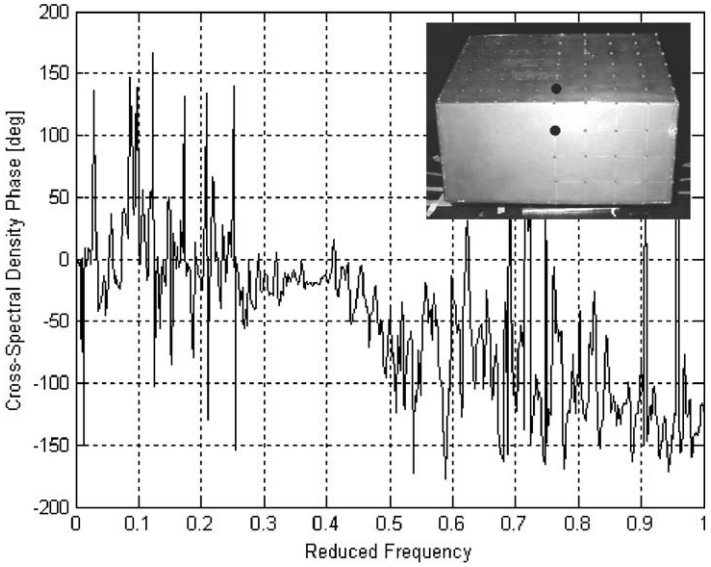

Fig. 23. Cross-spectral phase estimate between surface pressure taps on the slant and vertical base.

of Reynolds number, which result in well-defined separated shear layers at opposite sides of the wake that interact with one another, creating an alternate shedding.

Time-averaged results suggest that the flow over the slant mixes with the upper recirculation bubble behind the vertical base. Fig. 23 shows the correlation of shedding characteristics between pressure taps on the slant and upper region of the vertical base. At a reduced frequency of 0.39, the phase lag is close to 0°, suggesting in-phase shedding. Thus, the separations on the slanted edge shed simultaneously with the upper separation bubble on the vertical base. This result agrees well with flow visualization of Fig. 12 and time-averaged and unsteady surface pressures of Figs. 14 and 20, respectively, and emphasizes that the detached flow region on the slant and recirculation bubble on the vertical base are in fact a single large separated flow region. Thus, this new proposed flow topology is not limited to slant angles

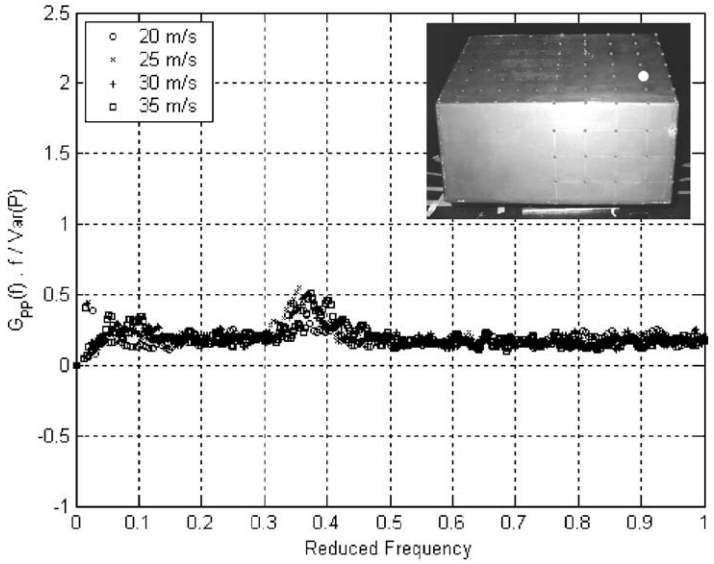

Fig. 24. Nondimensional auto-spectral density functions of a surface pressure tap located within the region of trailing vortex impingement on the slanted edge.

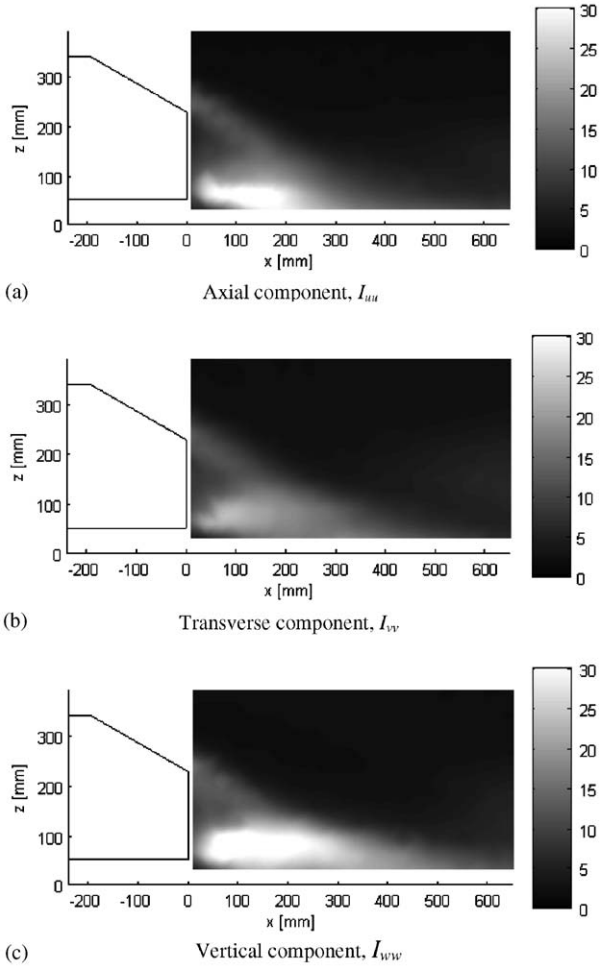

Fig. 25. Components of turbulence intensity measured in the wake along the plane of symmetry.

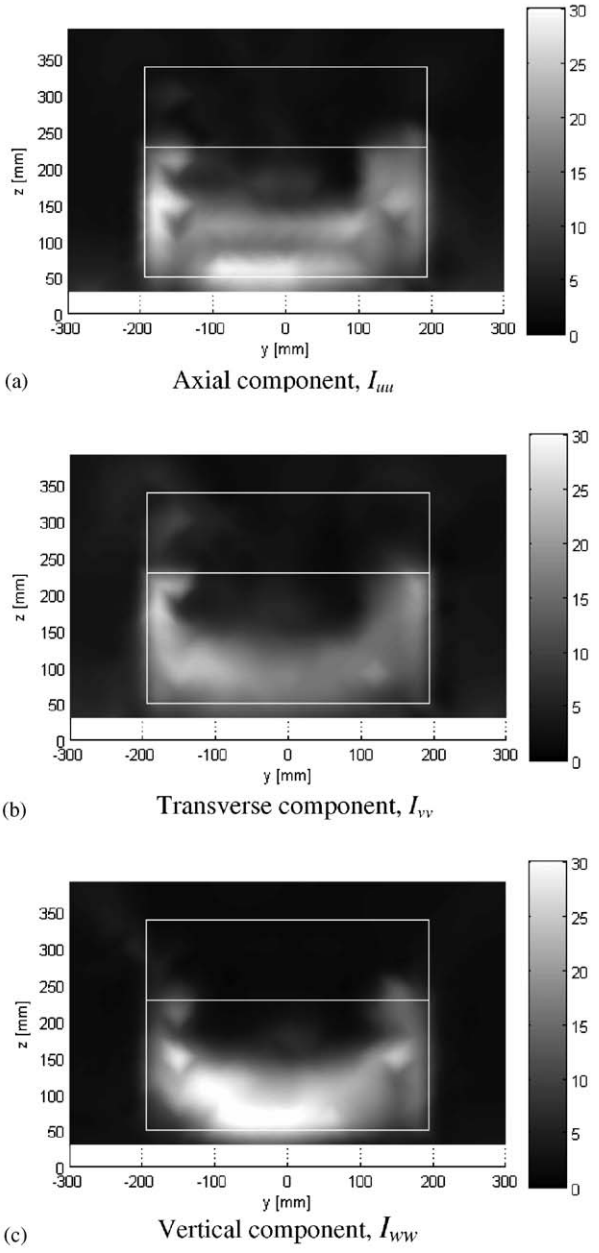

Fig. 26. Turbulence intensity measured in wake of model at a downstream transverse plane $x/L = 0.1$.

very close to and above the critical geometry, and is unlikely to be related to flow hysteresis. It is conjectured that the small phase lag of 20° between the taps is attributed to the time required for flow packets to move from the slant to the vertical base.

To understand the transient behaviour of the trailing vortex, an auto-spectral density function was taken for a pressure tap located within the vortex impingement region shown in Fig. 13. Fig. 24 shows that rather than a well-defined spectral peak, a small hump is observed centred at the same reduced frequencies as the vortex shedding behind the model, suggesting that the energy associated with the fluctuation is somewhat low. This suggests that the trailing vortices initiate in a relatively stable form, and are buffeted around further downstream as they interact with the highly unsteady flow behind the vertical base.

The downstream development of turbulence intensity along the plane of symmetry is shown in Fig. 25. Here, the components of turbulence intensity are expressed as a percentage and defined by

$$I_{ii} = \frac{\sqrt{\overline{i'^2}}}{U_\infty} = \frac{i_{\text{rms}}}{U_\infty}, \quad \text{where } i = u, v \text{ or } w. \tag{1}$$

From Fig. 25(a), small fluctuations along the centreline plane in the axial direction are observed in the flow separating from the slant, while the more intense fluctuations are exhibited behind the vertical base. In fact, Fig. 25(a) confirms earlier findings that the flow behind the vertical base undergoes a vortex shedding type phenomena in the axial direction. It is also evident that the region immediately behind the vertical base is relatively steady, with surface pressure fluctuations resulting from the shedding further downstream.

Fig. 25(b) shows that the turbulent fluctuations across the vertical centreline plane are significantly weaker, indicating that the vortex shedding described earlier is largely two-dimensional. Fig. 25(c) shows that the intense turbulent activity in the vertical direction is associated with the same region as the axial fluctuations (i.e. lower region behind the vertical base). Overall, Fig. 25 suggests that the vortex shedding behind the base is essentially a process of alternate stretching of each of the recirculatory bubbles as they fluctuate in both vertical and axial directions, with some turbulent activity also being exhibited across the wake in the transverse direction.

In order to further understand the time-dependant nature of the vortex structure, contours of axial, vertical, and transverse turbulence intensity are shown in Fig. 26, which are associated with a single downstream transverse measurement plane located inside the region of flow reversal.

Fig. 26 shows that the unsteady behaviour is particularly strong in both axial and vertical directions while lesser, albeit considerable, fluctuations occur in the transverse direction. The intense turbulence levels span across the majority of the model wake, assuming the shape of the large lower separation bubble behind the vertical base, finally terminating at the streamwise vortex cores at either side of the model.

Fig. 27 shows the spectral characteristics of a point (highlighted) located in the wake of the model, along the centreline, obtained at a test speed of 35 m/s.

Fig. 27 compares well to the turbulence intensity distributions shown above in that at this point in the flow, well-defined spectral peaks are evident for the axial and vertical velocity components, while a weaker spectral hump characterizes the transverse velocity component. These fluctuations correspond to a Strouhal number of about 0.4, comparing well to surface pressure fluctuations.

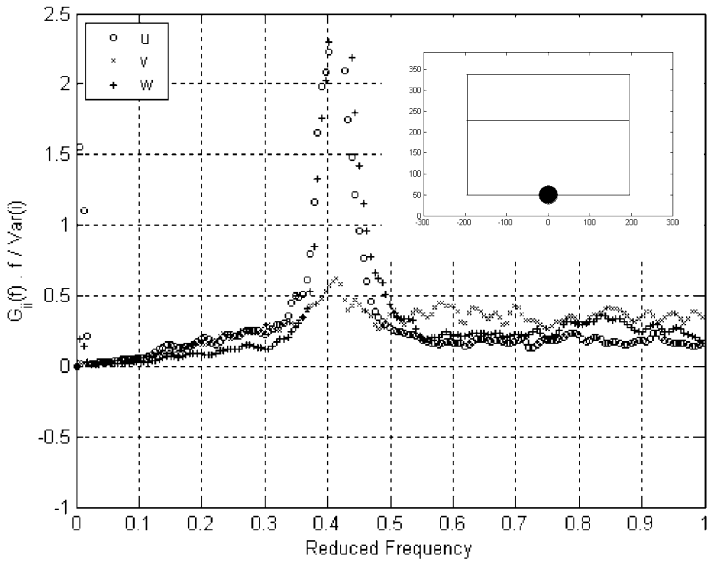

Fig. 27. Auto-spectral density of a selected point located at a downstream transverse plane $x/L = 0.1$ behind the vertical base.

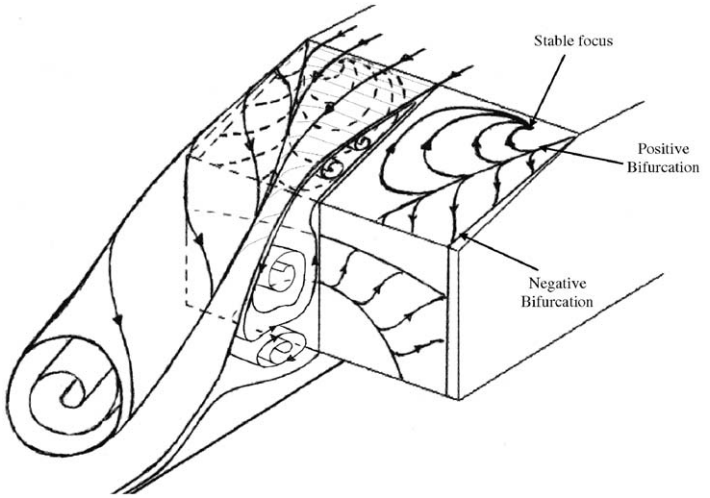

Fig. 28. Proposed topological flow structure of the Ahmed model with 30° rear slant.

4. Conclusion

The complex nature of the near- and far-wake of the Ahmed model geometry has been investigated, along with Reynolds number behaviour. It was found that although the model is quite bluff, drag coefficients exhibited some sensitivity to changes in Reynolds number; up to 15% reduction over the test speed range.

Far-wake time-averaged results compare well to previously published work, with the flow being characterized by a set of strong counter-rotating trailing vortices generated at the sides of the slanted edge.

Near-wake time-averaged flow structures showed that the flow above the vertical base was dominated by trailing vortices on either side of the model, which were located above a region of flow reversal, which was confined to the central region of the vertical base.

Smoke and oil flow visualization showed that the separated flow region over the slanted edge does not fully reattach further down the slant, but instead mixes with the large separated region behind the vertical base. This conclusion was further emphasized by the fact that the two regions consequently exhibited similar time-dependant behaviour. Compiling all time-averaged and transient results led to the flow patterns of Fig. 28, which are presented in a similar manner to the wake structures proposed by Ahmed et al. (1984).

Fig. 28 highlights all the important flow features found from this investigation, with surface patterns drawn as limiting streamlines (i.e. lines of surface shear stress) on the right hand side of the model, and off-body flows on the left—note that flow structures are not too scale. Clearly, the impingement of the trailing vortex along the C-pillar is shown. This impingement can be considered as a classic example of a positive bifurcation in terms of the 'critical point theory' described by Perry and Chong (1987) and Hornung and Perry (1984). Here, a streamline from the oncoming streamsurface (i.e. the trailing vortex surface) bifurcates into two at the line. On one side of this positive bifurcation, the flow tends toward a stable focus in a spiralling path, as it interacts with the flow reversals inside the detached flow region on the slant. On the other side, the path taken by the vortex as it interacts with the surface is shown. Note that the vortex separates at approximately 7° to the C-pillar. Although not found in results in this study, possibly due to limited resolution of flow maps, Spohn and Gillieron (2002) showed that a smaller, counter rotating, vortex existed above the small region between the line and C-pillar. As such, this 7° separation line can be viewed as a negative bifurcation, in which two streamlines appear to combine into one.

On the vertical base, the limiting streamlines indicate the path of the upper separation bubble, which causes significant levels of upwash on the surface. Note the arch shape made by the bubble as it extends to the sides of the model. No hypothesis is made for the regions above and below this bubble since results failed to reveal any definite path.

Off the body, the combination of the detached flow over the backlight and recirculation bubble on the vertical base is shown. It is important to note that although the detached flow region on the slanted edge only fails to reattach in the small region between the trailing vortices, it does reattach along the positive bifurcation lines. Also, it was found that this region was highly unsteady, so the time-averaged flow topology should only serve as an approximate

representation. Finally, the dominant trailing vortex generated at the C-pillar is also shown, with its path illustrating that the vortex core tends to move downward as it flows downstream.

Spectral characteristics of surface pressure signals revealed that the recirculation bubbles found behind the vertical base could be seen as analogous to longitudinal vortices in a von Karman vortex street.

The trailing vortices, which appear to dominate the far-wake, exhibit spectral behaviour similar to that of the recirculatory bubbles behind the vertical base, although with significantly lower energy levels. This suggests a strong interaction between the two flow regions, with the shedding characteristics of longitudinal vortices behind the base being transferred to the trailing vortices.

Finally, Reynolds number effects on spectral characteristics revealed that a drop in drag was accompanied by an increase in Strouhal number, comparing well with the vast amount of literature on bluff bodies.

References

Ahmed, S.R., Ramm, G., Faltin, G., 1984. Some salient features of the time-averaged ground vehicle wake. SAE 840300.

Bergh, H., Tidjeman, H., 1965. Theoretical and experimental results for the dynamic response of pressure measuring systems. National Aero and Aeronautical Research Institute NLR-TR F.238.

Chen, J., Haynes, B.S., Fletcher, D.F., 2000. Cobra probe measurements of mean velocities, Reynolds stresses and higher-order velocity correlations in pipe flow. Experimental Thermal and Fluid Science 21, 206–217.

Gilhome, B.R., 2002. Unsteady and Time-Averaged Near-Wake Flow Over the Rear of Sedan Automobiles, Ph.D. Thesis, Monash University.

Gilhome, B.R., Saunders, J.W., Sheridan, J., 2001. Time-averaged and unsteady near-wake analysis of cars. SAE 2001-01-1040.

Hooper, J.D., Musgrove, A.R., 1997. Reynolds stress, mean velocity, and dynamic static pressure measurement by a four-hole pressure probe. Experimental, Thermal and Fluid Science 15, 375–383.

Hornung, H., Perry, A.E., 1984. Some aspects of three-dimensional separation, Part 1: Streamsurface Bifurcations, Zeitschrift für Flugwissenschaften und Weltraumforschung 8, 77–87.

Iberall, A.S., 1950. Attenuation of oscillatory pressures in instrument lines. US Department of Commerce, National Bureau of Standards 45, RP2115.

Le Good, G., Garry, K.P., 2004. On the use of reference models in automotive aerodynamics. SAE 04B-25.

Mousley, P.D., Watkins, S., Hooper, J.D., 1998. Use of a hot-wire anemometer to examine the pressure signal of a high-frequency pressure probe, 13th Australasian Fluid Mechanics Conference. Monash University, Melbourne, Australia.

Nouzawa, T., Hiasa, K., Nakamura, T., Kawamoto, A., Sato, H., 1992. Unsteady analysis of the aerodynamic drag of notchback model with critical afterbody geometry. SAE 920202.

Perry, A.E., Chong, M.S., 1987. A description of eddying motions and flow patterns using critical-point concepts. Annual Review of Fluid Mechanics 19, 125–155.

Perry, A.E., Watmuff, J.H., 1981. The phase-averaged large-scale structures in three-dimensional turbulent wakes. Journal of Fluid Mechanics 103, 33–51.

Roshko, A., 1993. Perspectives on bluff body aerodynamics. Journal of Wing Engineering and Industrial Aerodynamics 49, 79–100.

Schlicting, H., 1960. Boundary Layer Theory. McGraw Hill Book Company, New York.

Sims-Williams, D.B., 2001. Self-Excited aerodynamic unsteadiness associated with passenger cars, Ph.D. Thesis, University Of Durham.

Sims-Williams, D.B., Dominy, R.G., 1998. Experimental investigation into unsteadiness and instability in passenger car aerodynamics. SAE 980391.

Spohn, A., Gillieron, P., 2002. Flow separations generated by a simplified geometry of an automotive vehicle. IUTAM Symposium on Unsteady Separated Flows, 8–12 April, Toulouse, France.

Vino, G., Watkins, S., 2004. A thirteen-hole probe for measurements in bluff body wakes, Fifth International Colloquium on Bluff Body Aerodynamics and Applications (BBAA5), July 11–15, Ottawa, Canada.

Wang, Q., Bearman, P.W., Harvey, J.K., 1996. A study of instantaneous flow structure behind a car by particle image velocimetry, Proceeding of IMechE Conference on Optical Methods and Data Processing in Heat and Fluid Flow, April 18–19, City University, London, pp. 179–188.

Watmuff, J.H., Perry, A.E., Chong, M.S., 1983. A flying hot-wire system. Experiments in Fluids 1, 63–71.